EES Batteries

PAPER

View Article Online
View Journal | View Issue

Cite this: *EES Batteries*, 2026, **2**, 529

Zinc oxide-reinforced silicon anodes for high-performance all-solid-state lithium-ion batteries

Renbo Liu,†[a] Chaolin Mi,†[a] Xiaobo Jiang,†[a] Shijian Xiong,[a] Zhengyang Song,[a] Yuanchang Shi,*[a] Xiaohang Lin,*[a] Peng Xiao,*[b] Longwei Yin[a] and Rutao Wang*[a,c,d]

Received 19th December 2025,
Accepted 25th January 2026

DOI: 10.1039/d5eb00238a

rsc.li/EESBatteries

Silicon is a promising candidate as an anode material for all-solid-state lithium batteries (ASSLBs) due to its high theoretical specific capacity (~3500 mAh g^{-1}), low cost and abundant earth reserves. Pioneering works find that the unique two-dimensional (2D) solid electrolyte interphase (SEI) layer formed between the pure Si electrode and solid-state electrolyte (SSE) can buffer the effect of the volume change of the Si anode; however, the poor kinetic performance of the Si anode caused by its lower Li^+ diffusion coefficient and electronic conductivity still hinders its practical implementation. Herein, an Si–ZnO composite anode is prepared by introducing ZnO nanoparticles into commercial Si microsheets. ZnO spontaneously transforms into a Zn/Li_2O mixture during the initial electrochemical cycling with Li^+. The formed Zn/Li_2O mixture with a mixed ion- and electron-conducting property enables the uniform lithium-ion flux distributions at interfaces, thereby improving the rate capability and cycling stability of the Si anode significantly. The Si–ZnO composite anode delivers a reversible capacity of 2349 mAh g^{-1} at 0.1 A g^{-1} and yields a discharge capacity of 1125 mAh g^{-1} at a high rate of 5 A g^{-1}. Furthermore, ASSLBs based on the Si–ZnO anode exhibit superior rate capability and robust cycling performance.

Broader context

The global transition to clean energy and electric transportation urgently requires safer, high-energy batteries. This work tackles the core challenges in extending the range of electric vehicles and improving grid storage by creating anodes that store more energy, moving us toward a sustainable future. We specifically addressed the major drawbacks of silicon, a high-capacity material that unfortunately suffers from poor performance under fast charging due to slow lithium-ion diffusion and poor electronic conductivity. Our key finding is that adding zinc oxide to silicon creates a unique, self-forming structure. This structure efficiently promotes the fast transmission of lithium ions, enabling the silicon anode to perform exceptionally well even at very high charging speeds. This breakthrough is significant because it provides a practical path to commercialize silicon anodes. It directly impacts battery manufacturers and the electric vehicle industry by promising fast-charging, long-lasting batteries, thereby accelerating the adoption of clean energy technologies.

Introduction

All-solid-state lithium batteries (ASSLBs) are regarded as promising candidates for next-generation lithium-ion batteries (LIBs) due to their potentially higher safety and energy density than their conventional liquid counterparts.[1–3] However, achieving high-energy-density ASSLBs is largely dependent on the development of high-capacity anode materials in a solid-state architecture. Currently, extensive studies are conducted on Li metal anodes due to their high theoretical capacity (3860 mAh g^{-1}) and low electrochemical potential (−3.04 V *vs.* the standard hydrogen electrode).[4] However, severe interfacial instability problems between the lithium metal anode and solid-state electrolytes (SSEs), such as dendrite growth and void generation, have seriously prevented their further utilization.[5–7,46] In contrast, the alloy-type Si anode has a moderate electrochemical reduction potential (0.4 V *vs.* Li^+/Li) and a high theoretical specific capacity (3579 mAh g^{-1}), enabling it to achieve a high energy density close to lithium metal anode-based batteries.[8,9] Unlike lithium metal anodes, which store energy through the deposition and stripping of Li^+, Si anodes

[a]*Shandong Provincial Key Laboratory of Electrochemical Catalysis and Conversion, State Key Laboratory of Coatings for Advanced Equipment, School of Materials Science and Engineering, Shandong University, Jinan 250100, China. E-mail: rtwang@sdu.edu.cn, yuanchangshi@sdu.edu.cn, lxh12345@sdu.edu.cn*
[b]*State Grid Jiangsu Electric Power Co., Ltd Research Institute, Nanjing 211103, China. E-mail: xiaop1@js.sgcc.com.cn*
[c]*Key Laboratory of Advanced Energy Materials Chemistry (Ministry of Education), Nankai University, Tianjin 300071, China*
[d]*Shandong Laboratory of Advanced Materials and Green Manufacturing at Yantai, Yantai 264003, China*
†These authors contributed equally to this work.

are alloyed with Li^+ at 0.4 V *vs.* Li^+/Li, thereby preventing the problem of lithium dendrite growth. Owing to the abundance, low-cost, and environmentally friendly properties of Si, Si anodes can be manufactured on a large scale.[10] Therefore, Si-based ASSLBs are considered more practical in terms of electrochemical performance and commercialization.

In an all-solid-state architecture, the electrochemical and mechanical behaviors of the silicon anode are apparently different from those of the liquid system. The silicon anode in ASSBs forms a two-dimensional (2D) solid electrolyte interphase (SEI) layer with the SSE.[11] This 2D SEI prevents the continuous contact of newly-generated interfaces with the SSE due to volume changes, thereby avoiding the problem of SEI overgrowth.[12] By contrast, Si anodes undergo continuous SEI formation in liquid electrolytes, resulting in severe lithium loss and pulverization during cycling.[13,14] Although a passivating SEI formed on Si anodes provides a prerequisite for the practical application of Si-based ASSLBs, Si anodes still face a severe volume change (>300%), long-range Li^+ diffusion path, low Li^+ diffusion coefficient and poor electronic conductivity, hindering their further development.[47–49]

To circumvent these issues, the most intuitive and commonly used approach is the use of composite anodes composed of Si and SSE, which change the contact area between Si and SSE from 2D plane to three-dimensional (3D) interspace, thereby shortening Li^+ diffusion paths and enhancing the rate capability of Si anode.[15] Hu *et al.*, however, found that the 3D contact between Si and SSE would accelerate the growth of SSE at the Si/SEE interface,[11] potentially resulting in several resistance increase in composite anodes as well as fast capacity decay. The introduction of conductive carbons (*e.g.*, hard carbon and graphite) is also frequently employed to accommodate large volume change and increase the electronic conductivity of Si anodes.[16–18] Unfortunately, conductive carbons and SSEs (*e.g.*, sulfide SSEs) are always incompatible as their integration promotes SSE decomposition and Li metal plating.[16,19,20] Besides, introducing high-strength copolymer with an ionic-electronic dual conductive function was proposed to restrain the large volume change and facilitate the uniform diffusion of Li ions.[21] Nevertheless, this ideal solution is built on the incorporation of Ag nanoparticles to realize the ionic-electronic dual conductive function, increasing the cost. Therefore, designing a suitable composite structure with the properties of ionic-electronic dual conductivity and low cost is critical for the practical implementation of Si anode based on ASSLBs.

In this study, we introduced nano-sized ZnO into Si microsheets to improve the rate capability and cycling performance of Si anode. The Si–ZnO/Li–In half-cell results show that the well-designed Si–ZnO composite anode can reversibly charge/discharge at a high current density of 5 A g^{-1} with a high specific capacity of 1125 mAh g^{-1}, which are approximately two times higher than those of pure Si anode. ASSLBs, fabricated with the Si–ZnO anode, $LiNi_{0.8}Co_{0.1}Mn_{0.1}O_2$ (NCM811) cathode, and $Li_{5.5}PS_{4.5}Cl_{1.5}$ SSE, exhibit a discharge specific capacity of 185 mAh g^{-1} at 0.1C and are able to stably cycle for more than 200 cycles at 0.5C with a capacity retention rate of 71%. The enhanced rate capability and cycling stability of Si-ZnO||NCM811 full cells is largely associated to that introducing ZnO enables the uniform lithium-ion flux distributions at interfaces due to the *in situ* formation of a mixed ion- and electron-conducting Zn/LiZn and Li_2O mixture, as confirmed by the combined *ex situ* structural and *in situ* electrochemical analyses. Our study provides an efficient and low-cost production method for high-performance Si composite anodes, potentially accelerating the advent of the large-scale industrial fabrication of Si anode-based ASSLBs.

Results and discussion

Si–ZnO_x composites (x = 2, 4, and 8, where x represents the mass ratio of zinc acetate/Si precursors) were synthesized by evaporating the zinc acetate and commercial Si mixture, followed by heating at 700 °C, as schematically shown in Fig. 1a. Fig. 1b shows the X-ray diffraction (XRD) patterns of the Si–ZnO_x and Si samples. These peaks located at 28.4°, 47.3°, and 56.1° are the characteristic diffraction peaks of crystalline Si, which correspond to the (111), (220), and (311) crystal planes, respectively. In addition to the diffraction peaks of Si, several weak diffraction peaks at 31.7°, 34.4°, 36.3° and 62.9° were found in the Si–ZnO_4 sample, which can be assigned to the (100), (002), (101) and (103) planes of ZnO. The diffraction peak intensity of ZnO in the Si–ZnO composites gradually increased with the increasing mass ratio of zinc acetate/Si during synthesis.

The scanning electron microscopy (SEM) images presented in Fig. 1c and d demonstrate that the microsheet-like morphology of Si shows no apparent change after the introduction of ZnO. However, the Si–ZnO sheets exhibit a rough surface, whereas the Si sheets demonstrate a smooth surface, suggesting the anchoring of ZnO nanoparticles onto the Si sheets. The energy-dispersive spectroscopy (EDS) images in Fig. S1 show the uniform distribution of the Si, Zn and O elements in the Si–ZnO_4 sample, indicating the successful synthesis of the homogeneous Si–ZnO_4 composites. The transmission electron microscopy (TEM) images in Fig. 1e and the corresponding EDS mapping in Fig. S2 reveal that ZnO nanoparticles are distributed on the surface of the Si sheets. The typical high-resolution TEM image of Si–ZnO_4 in Fig. 1f shows clear lattice stripes belonging to Si and ZnO crystals. Specifically, the lattice stripe with a spacing of 0.31 nm in Fig. 1g corresponds to the (111) crystalline plane of cubic Si crystals, and the lattice stripe with a spacing of 0.26 nm in Fig. 1h is consistent with the (002) crystalline plane of hexagonal ZnO crystals. Notably, between the ZnO particles and Si, a banded region presenting an amorphous structure are found, which corresponds to the oxide layer (SiO_x) on the surface of the Si particles.

X-ray photoelectron spectroscopy (XPS) was performed to reveal the surface chemical composition of the Si–ZnO_4 sample. The full-scale XPS survey spectra in Fig. S3a show that apart from Si 2p, Si 2s, O 1s and C 1s, several additional peaks around ~500 eV and ~1045.3 eV assigned to Zn Auger and Zn

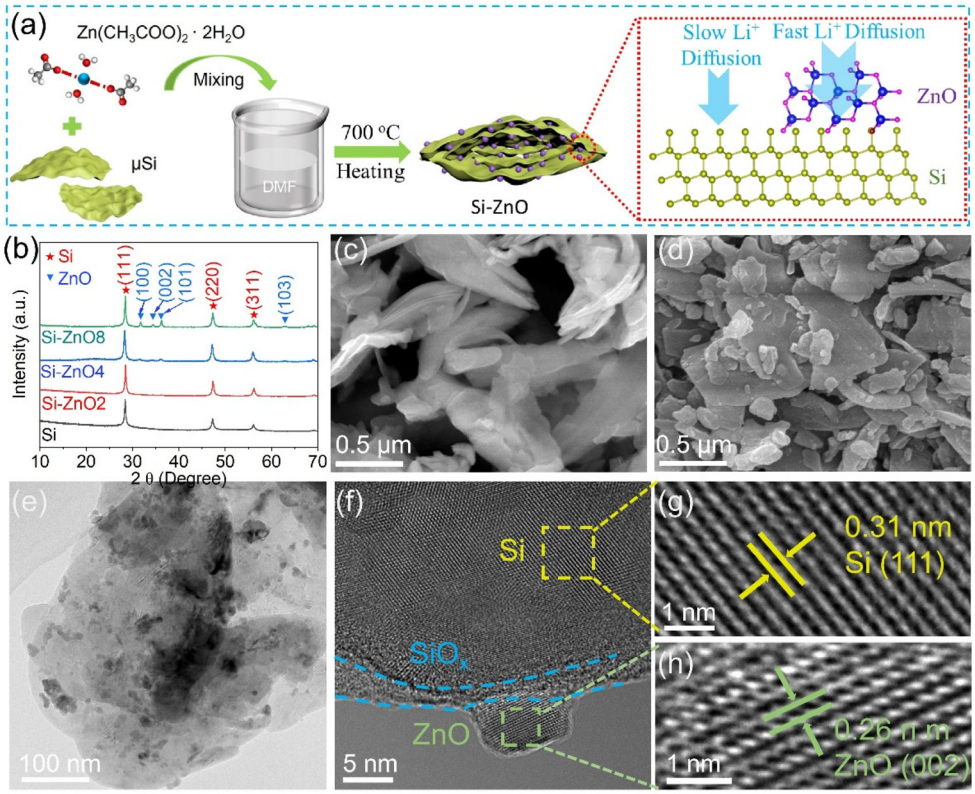

Fig. 1 Structure of the Si–ZnO_4 anode. (a) Schematic of the preparation of the Si–ZnO_4 composites. (b) XRD pattern of the Si–ZnO and pure Si samples. SEM images of commercial pure Si (c) and Si–ZnO_4 (d). (e) TEM images of Si–ZnO_4. (f) HRTEM images of Si–ZnO_4 and the lattice stripes of Si (g) and ZnO (h).

2p are found in the Si–ZnO sample, respectively, further confirming the co-existence of the Si and Zn elements in the composite sample. In the high-resolution Si 2p spectrum of the Si–ZnO_4 composite (Fig. S3b), the two peaks located at 98.9 eV and 103 eV correspond to Si 2p and Si–O, respectively, which is highly identical with that of the pure Si sample. The high-resolution O 1s spectrum of the Si–ZnO_4 sample (Fig. S3c and Fig. 3d) can be deconvoluted to the fitted peaks of Si–O and Zn–O. By comparison, no sign of Zn–O bonding is observed in the O 1s spectrum of the pure Si sample. The peak of Si–O bonding originates from the oxide layer (SiO_x) on the surface of Si particles, which is confirmed by TEM observation. ZnO accounts for ~11.6 wt% of the Si–ZnO_4 composite (deducing from the stoichiometric ratio of Si and zinc acetate during the experiment), which is close to the XPS (~13.6 wt%) and EDS (~10.9 wt%) tests.

The electrochemical performance of the Si and Si–ZnO anodes was initially investigated in a half-cell at 60 °C, which used a Li–In alloy (0.6 V *vs.* Li^+/Li) as the counter/reference electrode. Fig. 2a comparatively shows the initial galvanostatic charge and discharge curves of the Si and Si–ZnO_4 anodes under a current density 0.1 A g^{-1}. These two initial discharge curves are composed by a voltage drop area and a long discharge plateau.

Pure Si anodes showed an apparent inflection point between the voltage drop area and the discharge plateau area, which was largely due to the sluggish Li-ion diffusion and electron transfer on non-lithiated Si anode.[21] By contrast, Si–ZnO_4 experienced a relative smooth change between the voltage drop area and the discharge plateau area, suggesting enhanced ion diffusion and electron transfer. Notably, the specific capacity of the Si–ZnO_4 anode contributed from the voltage drop area was much higher than that of the Si–ZnO_4 anode. The additional capacity from the voltage drop area for Si–ZnO_4 was probably due to the lithiation into ZnO with a higher redox potential than the lithiation into Si.[22,23] The Si–ZnO_4 anode yielded the initial discharge and charge capacities of 2907 and 2218 mAh g^{-1}, respectively, displaying lower initial capacities than the pure Si anode. The reduced specific capacity in Si–ZnO_4 was directly related to the reduced mass ratio of Si in the Si–ZnO_4 composite. The initial coulombic efficiency (ICE) of Si–ZnO_4 was calculated to be 76.3%, which was close to that of pure Si (77.8%). Although the introduction of ZnO into Si induced negligible effects on the improvement of specific capacity and ICE at a low rate, a large improvement in specific capacity and rate capability was achieved for the Si–ZnO anode as the rate increased to 0.8 A g^{-1} or higher (Fig. 2b). For example, the Si–ZnO_4 anode delivered a reversible discharge capacity of 2042 mAh g^{-1} at 0.8 A g^{-1}, whereas the specific capacity of the Si anode rapidly decreased to 1483 mAh g^{-1} at the same rate level. As the charge/discharge

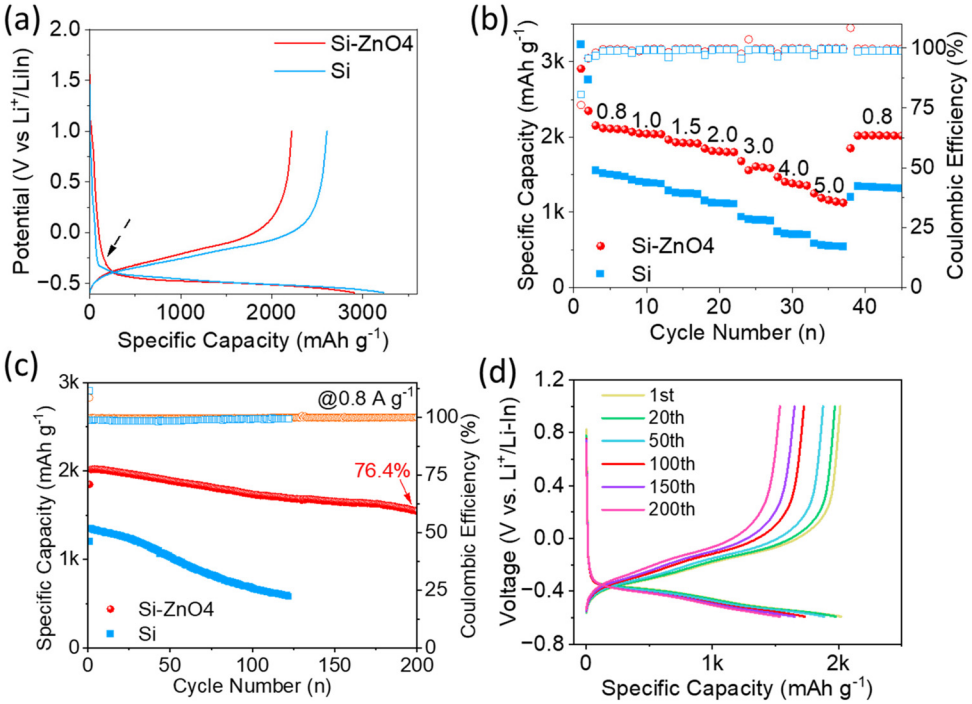

Fig. 2 Electrochemical performance of the Si–ZnO_4 anode half-cell at 60 °C. (a) Initial galvanostatic charge and discharge profiles of the Si–ZnO_4 and pure Si anodes. (b) Rate performance of the Si–ZnO_4 and pure Si anodes in half-cell. (c) Long-term cycling performance of the Si–ZnO_4 half-cell at 0.8 A g^{-1} and (d) the corresponding galvanostatic charge and discharge profiles of the Si–ZnO anode at different cycles.

current density increased to 5 A g^{-1}, the Si–ZnO_4 anode still delivered a specific capacity of 1123 mAh g^{-1}, which was approximately two times higher than that of the pure Si anode. Fig. S4 shows that the Si–ZnO_4 anode has a better rate performance than the other Si–ZnO_x anodes; thus, it was selected for further studies.

Fig. 2c provides a comparison of the long-term cycling performance of the Si–ZnO_4 and Si anodes at 0.8 A g^{-1}. The Si–ZnO_4 anode yielded a specific capacity of 1554 mAh g^{-1} after 200 cycles, with a capacity retention of 76.4%. In contrast, pure Si underwent rapid decay in capacity after 120 cycles, indicating poorer cycling performance than the Si–ZnO_4 anode. Fig. 2d further shows that no instability phenomenon such as soft-short circuit was observed in the galvanostatic charge and discharge curves of Si–ZnO_4 during the whole cycles. The capacity decay for Si–ZnO_4 was largely related to the gradually increasing interface impedance and the step-down Li^+ diffusion within the Si electrode during the long-term cycles, as suggested by electrochemical impedance spectroscopy (EIS) performed at the different cycling states (Fig. S5). The enhanced rate capability of Si-ZiO_4 was still preserved at room temperature (Fig. S6). Even at a high rate of 4 A g^{-1}, the Si-ZiO_4 anode still yielded a specific capacity of 880 mAh g^{-1}. In contrast, the pure Si anode appeared hardly capable of charging/discharging at the same rate level.

To further investigate the reaction mechanism during the alloying process of the Si–ZnO_4 anode, *ex situ* XRD was initially employed. In the pristine state, only the diffraction peaks of crystalline Si (c-Si) and ZnO appeared in the XRD pattern (Fig. 3a). After the first discharge process (lithiation), the main peaks of crystalline Si and ZnO nearly disappeared. Meanwhile two broad peaks at 23.1° and 41.1° were observed in the sample, which were close to the (111) and (321) crystal planes of the $Li_{13}Si_4$ alloy,[24] respectively. These two broad peaks confirmed the phase transformation of crystalline silicon (c-Si) to lithium silicides (Li_xSi). In contrast, no significant LiZn alloy diffraction peaks were observed in the pattern, which was probably due to the low mass ratio of ZnO in the Si–ZnO_4 sample and the location of the main LiZn alloy diffraction peaks close to the diffraction peaks belonging to $Li_{13}Si_4$. A weak peak around 28.4° indicated residual c-Si in the Si–ZnO_4 anode without lithiation. After the first charging (delithiation), the peaks belonging to $Li_{13}Si_4$ disappeared, and the diffraction peaks of crystalline ZnO never reappeared. As several weak diffraction peaks around 28.5°, 47.3°, and 56.2° assigned to the residual c-Si were still detected, amorphous Si (a-Si) was formed preferentially after delithiation.[25] Notably, a new peak appeared at 43.1°, corresponding to the (101) plane of Zn, suggesting the delithiation of LiZn to Zn. Several weak peaks around 30°–35° that appeared in the XRD patterns of the Si–ZnO anode after the lithiation and delithiation stages were largely due to the residual Si, LPSCl electrolyte and its decomposed products during a short exposure to air.[12]

To further determine the phase transformation of the Si–ZnO anode during the initial lithiation/delithiation process, *ex situ* Raman analysis was performed on the Si–ZnO anode. Fig. 3b

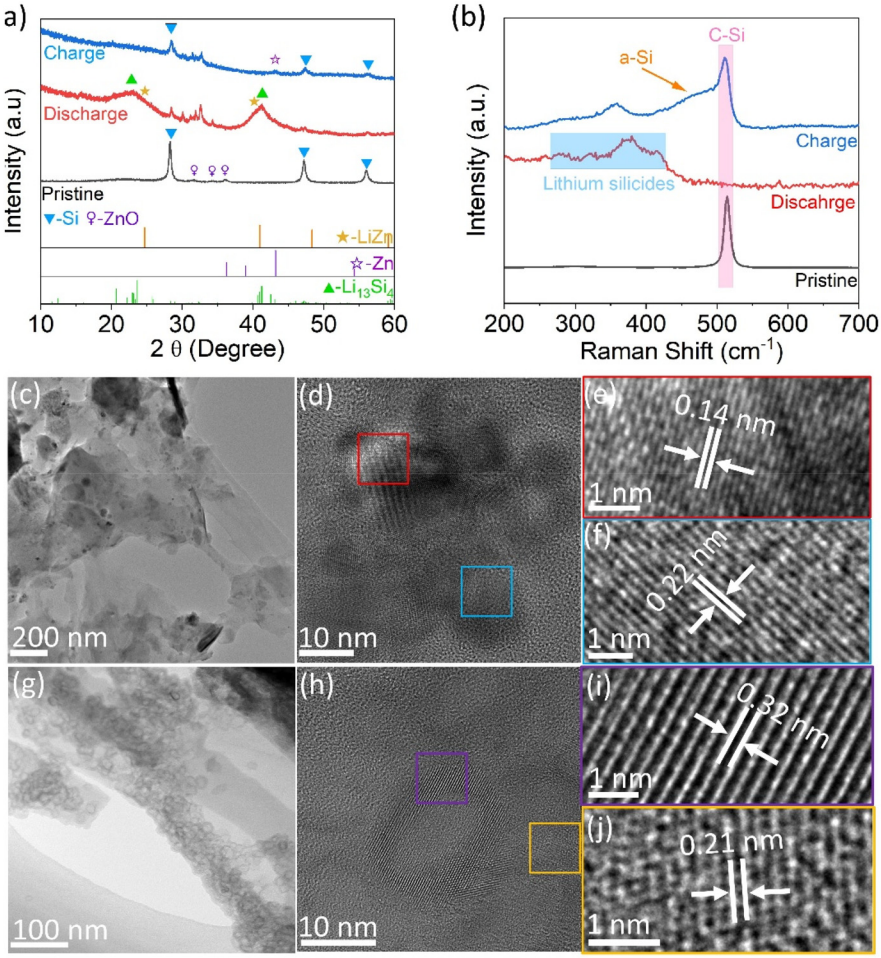

Fig. 3 Structural change in the Si–ZnO_4 anode during the initial lithiation and delithiation processes. (a) Ex situ XRD patterns of the Si–ZnO_4 anode. (b) *Ex situ* Raman spectra of the Si–ZnO_4 anode. (c) and (d) TEM image of Si–ZnO_4 after the initial discharge state. (e) and (f) Magnified HRTEM images in red and blue boxes in (d), showing the lattice stripes of $Li_{13}Si_4$ (321) and LiZn (331), respectively. (g) and (h) TEM image of Si–ZnO_4 after the initial charge state. (i) and (j) Magnified HRTEM images in purple and yellow boxes in (h), showing the lattice stripes of Si (111) and Zn (101), respectively.

shows that the sharp peak of c-Si around 514 cm^{-1} observed in the pristine electrode completely disappeared after the initial lithiation; in contrast, one prominent peak around 375 cm^{-1} coupled with three weak peaks around 280 cm^{-1}, 320 cm^{-1}, and 415 cm^{-1} appeared, which could be assigned to lithium silicides, such as $Li_{13}Si_4$ and $Li_{21}Si_5$.[26] After the delithiation process, the previous peaks corresponding to lithium silicides disappeared, while a sharp peak assigned to c-Si and a bump assigned to a-Si (centered around 467 cm^{-1}) were detected in the Raman spectra, suggesting the dealloying of lithium silicides to Si. Due to the low mass ratio of ZnO in the Si–ZnO composite, the signals of ZnO, Zn, or LiZn were not detected by Raman spectroscopy.

The *ex situ* TEM measurements of the Si–ZnO_4 anode at the initial lithiation/delithiation state were employed to further confirm the phase transformation. At the full lithiation state, the pristine microsheet-like morphology of Si–ZnO_4 was still preserved (Fig. 3c). The HRTEM images in Fig. 3d–f show two different lattice stripes with spacings of 0.22 nm and 0.14 nm belonging to the (321) crystal plane of $Li_{13}Si_4$ and the (331) crystal plane of the LiZn alloy, respectively, confirming the alloying reactions of Si to lithium silicides and Zn to LiZn. At the full delithiation state of 2.0 V, many round cavities were found on Si microsheets (Fig. 3g), which is consistent with other studies on the conversion of crystalline Si nanoparticles to a porous structure in a liquid organic electrolyte.[27–29] The HRTEM image in Fig. 3h shows that the c-Si cavities are surround by a-Si. These cavities are mainly composed of c-Si with a wall thickness of ~5 nm, as indicated by the clear lattice stripe with a spacing of 0.32 nm, which corresponds to the (111) crystal plane of Si (Fig. 3i). Besides, a trace of Zn can be found in the HRTEM image of Fig. 3j, as suggested by a lattice fringe of 0.21 nm belonging to the (101) crystal plane of metal Zn. The EDS mapping in Fig. S7 further confirmed that Zn atoms were still highly dispersed in the Si–ZnO electrode after the charge/discharge process.

Based on the above discussion, the lithium-ion charge storage mechanism for the Si–ZnO composite is proposed as below. During the initial lithiation, c-Si in the Si–ZnO composite would be transformed into lithium silicides (*e.g.*, $Li_{13}Si_4$), whereas ZnO

would be transformed into Li_2O and LiZn. During delithiation, lithium silicides would be changed into a-Si, whereas LiZn would be transformed into Zn rather than ZnO. In fact, ZnO could be observed on the a-Si substrate when the delithiated Si–ZnO_4 sample was exposed to air for a long time (Fig. S8). Recent studies have found that the formed LiZn alloy in intermediate layers enabled the uniform lithium-ion flux distributions at interfaces.[30,31] Hence, the generation of metal Zn or Li–Zn alloy may promote electron and ionic transfers in the Si anode and enhance the kinetic performance of the Si anode.[31–33] Besides, the formed Li_2O is a good conductor of Li^+,[34–36] which can enhance the conduction of Li^+ in the Si anode.

To visualize the morphologic evolution of Si–ZnO_4, we obtained the cross-sectional and top-view SEM images of the pristine, lithiated, and delithiated Si–ZnO_4 anodes (Fig. 4a–f and Fig. S9). In the pristine state, clear boundaries between the Si–ZnO_4 microsheets could be observed in the, and some voids were distributed in the electrode (Fig. 4a and d). After the lithiation, the Si–ZnO_4 electrode tended to be dense, with most voids disappearing between the pristine Si–ZnO_4 microsheets (Fig. 4b). In addition, the original particle boundaries of the Si–ZnO_4 electrode vanished. An enlarged SEM image in Fig. 4e shows that the entire Si–ZnO_4 electrode has become interconnected and densified lithium silicides. After delithiation, the Si–ZnO_4 electrode did not recover its original discreet microsheets, with voids between them. Instead, the Si–ZnO_4 microsheets tended to coalescence into bulk electrode, with few vertical cracks appearing (Fig. 4c and f). These cracks are largely related to interfacial stress concentration and delamination caused by excessive volume expansion, which may be responsible for capacity decay during the followed cycles. The EDS images in Fig. S10 and S11 show that Zn atoms are homogenously distributed on the Si–ZnO_4 electrode during the lithiation and delithiation, suggesting no apparent phase separation. Besides, there were no evidences of SEI or solid-state electrolyte between each lithiated or delithiated microsheets.

We further qualified the thickness change of the Si–ZnO_4 electrode during lithiation and delithiation. In the pristine

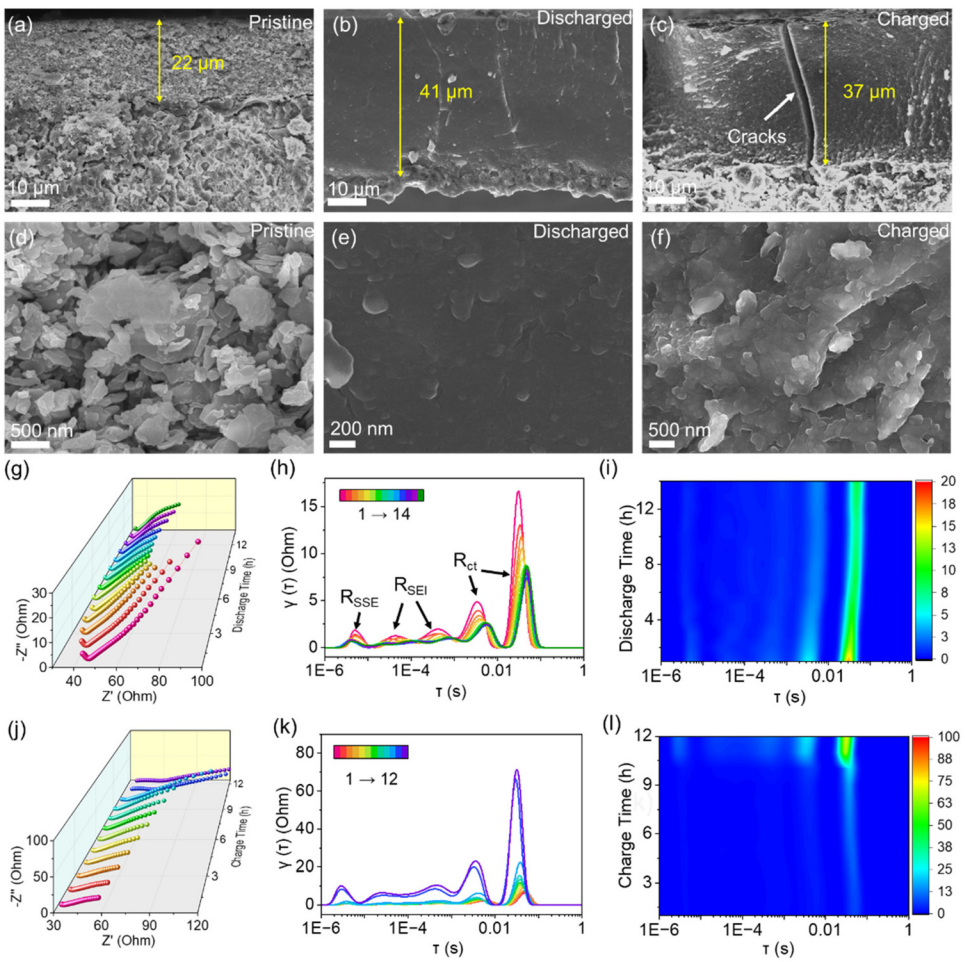

Fig. 4 Cross-section SEM images of the Si–ZnO_4 anode at the (a) pristine state, (b) initial discharged state, and (c) initial charged state. (d–f) Corresponding magnified cross-section SEM images of the Si–ZnO_4 anode at these three states. (g) EIS curves of the Si–ZnO_4 anode in half-cell during discharging at 0.2 A g^{-1} and the corresponding DRT curves (h) and DRT contour map (i). (j) EIS curves of the Si–ZnO_4 anode in half-cell during charging at 0.2 A g^{-1} and the corresponding DRT curves (k) and DRT contour map (l).

state, the thickness of the electrode was about 22 μm. After the alloying process of the Si–ZnO_4 anode, the thickness of the electrode increased to approximately 41 μm, with a volume expansion of 86.4%, which falls short of the pure Si growth value (285%, Fig. S12). Difference in expansion rate is mainly associated to that the expanded Si microsheets gives priority to fill the voids between original discreet microsheets under a high impressed pressure, which provides a plausible explanation on the densified electrode with few voids shown in the beforementioned SEM image (Fig. 4b and e). After delithiation, the thickness of the Si–ZnO_4 electrode decreased to ~37 μm, which was still thicker than that in the pristine state. The TEM images in Fig. 3g find that many cavities formed on Si–ZnO_4 microsheets after delithiation may support the expanded volume, which are responsible for limited shrink in thickness as compared with the lithiated state. The 22-41-37 μm thickness change law for our Si–ZnO_4 during the lithiation and delithiation is highly identical with Meng's group work on pure Si electrode.[12] The large volumetric change is considered as the chief culprit for capacity decay during cycling, which may be alleviated by introducing the carbon matrix or utilizing the high-strength binder.[17,21]

We further employed *in situ* galvanostatic electrochemical impedance spectroscopy (GEIS) with distribution of relaxation time (DRT) analysis to reveal the interfacial impedance change and interfacial charge transfer evolution of the Si–ZnO_4 electrode. During the first lithiation, the internal impedance and charge transfer impedance of the Si–ZnO_4 anode exhibited a gradual decrease with increased discharge time (Fig. 4g), suggesting a gradual increase in the ionic and electronic conductivities of the Si–ZnO_4 electrode. DRT was then employed to analyze multiple charge transfer processes elaborately in electrodes by transforming.

EIS into characteristic distributions based on time scales.[6,37] As shown in Fig. 4h and i, five peaks with different relaxation time constants (τ) can be observed in the DRT curves. At the beginning of lithiation, the intensity of the peak around 10^{-5}–10^{-6} s (denoted as R_{SSE}) decreased and had a slight shift to the high-frequency region, which could be attributed to the decomposition of the electrolyte at the interface with electrode due to side reactions. This peak, however, remained essentially unchanged during the subsequent discharge process, indicating the stabilized electrolyte. The peaks at 10^{-3}–10^{-4} s (denoted as R_{SEI}), which represent the formation of the SEI layer, gradually decreased throughout the discharge process and then stabilized at the final stage, indicating the formation of SEI during the first lithiation process. The two peaks at 10^{-1}–10^{-3} s (denoted as R_{ct}), corresponding to the charge transfer of the alloying process, showed a similar change to SEI. This could also be explained by the significant enhancement in the ionic and electronic conductivity caused by the formation of lithium silicides and the close contact between Si microsheets caused by the large-volume change, which in turn enhanced the kinetic properties of the electrode and accelerated the charge transfer process.

In the delithiation, a highly reversible process was found on the EIS and DRT curves. As shown in Fig. 4j–l, the overall charge transfer impedance of the electrode gradually increases along with the increasing charge time. No apparent change in the peak around 10^{-5}–10^{-6} s was observed in the DRT curves, suggesting a stable electrolyte. The peaks belonging to the SEI layer of the lithium silicides showed only a small change, which could be attributed to the 2D SEI interface between the electrode and the solid-state electrolyte. The SEI layer gradually stabilized as the reaction proceeded without the issue of constant formation on the newly exposed surface. However, the intensity of the two peaks representing Si alloying increased with the sustained delithiation process. Moreover, a surge in charge transfer impedance was observed at the end stage of delithiation. This was largely due to the transformation from lithium silicides with high ionic and electronic conductivities into a-Si with poor ionic and electronic conductivities as well as the volumetric shrinkage on the Si–ZnO_4 electrode (Fig. 4c). A similar interfacial charge transfer evolution was found on pure Si anode during the initial lithiation and delithiation (Fig. S13). By contrast, pure Si electrode displayed higher charge transfer resistances than the Si–ZnO_4 electrode at the initial lithiation stage and the final delithiation stage (Fig. S13), which suggests that the introduction of ZnO enables the uniform lithium-ion flux distributions at interfaces due to the beforehand formation of a mixed ion- and electron-conducting Zn/LiZn and Li_2O mixture. Nevertheless, at the final lithiated stage and the initial delithiated stage, the pre-formed lithium silicides with high Li atomic loading have higher ionic and electronic conductivities in nature than pure Si, which may play a dominant role in ionic and electronic transfer. We also found that both the internal impedance from grain boundary and SEI and charge transfer impedance from the alloying reaction for the Si–ZnO_4 electrode increased significantly after multiple cycles (Fig. S14), providing a plausible explanation on capacity decay during the cycle.

To clarify the underlying reason for the fast kinetics of Li^+ transport on Si–ZnO, density functional theory (DFT) calculations were employed. According to the above TEM results, the exposed surfaces of Si and ZnO were mainly the Si(111) and ZnO (001) surfaces, respectively. Therefore, in subsequent calculations, we mainly focused on the diffusion behavior of Li^+ on the Si(111) surface and across the heterojunction formed between the Si(111) and ZnO(001) surfaces. For the Si(111) surface, the famous Si(111)-(7 × 7) reconstruction structure (Fig. S15) has been considered.[38] This structure is known as the Dimer–Adatom stacking-fault (DAS) model. It is characterized by twelve adatoms on the top layer and six rest atoms. Additionally, it features a stacking fault in one of the two triangular subunits of the second layer, nine dimers at the borders of these triangular subunits in the third layer, and a deep corner hole at each apex of the surface unit cell. In this study, the dangling bonds of silicon on the fixed-atom side of the DAS structure were saturated with hydrogen. For the Si/ZnO interface, four possible heterojunction structures have been simulated (Fig. 5a inset). The most stable structure at which a reconstruction occurs was con-

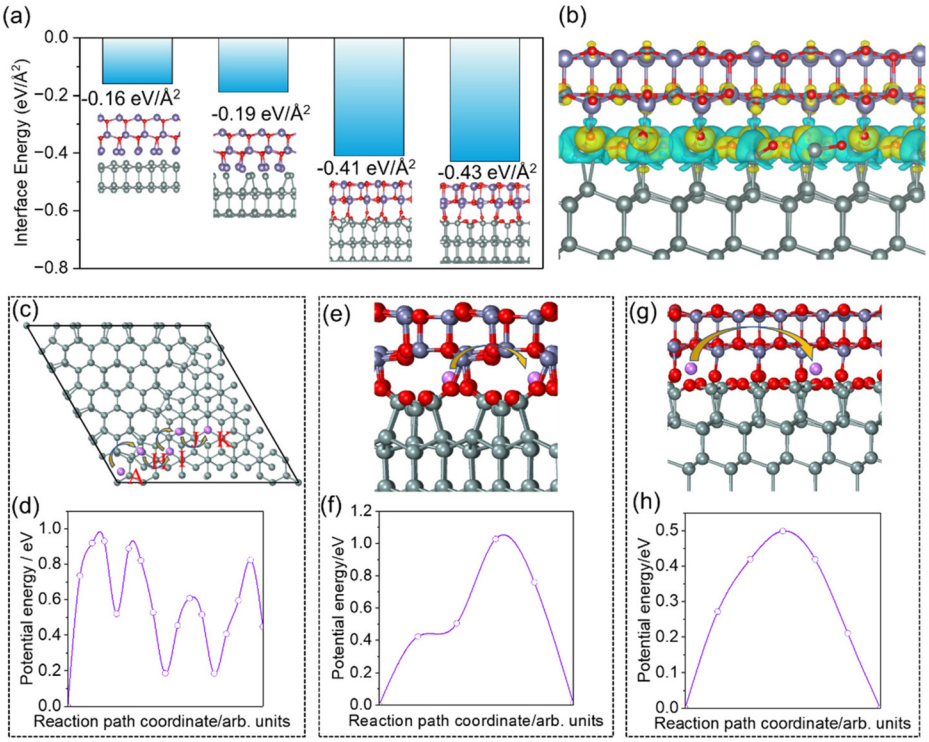

Fig. 5 DFT calculation on the Si/ZnO interface. (a) Four simulated heterojunction structures of Si–ZnO and the corresponding interface energies. (b) Charge density difference of the Si/ZnO interface. The accumulation of electron density is plotted in yellow, and charge depletion is plotted in blue. (c) Diagram showing one of the possible Li^+ diffusion paths on Si (111) and (d) the corresponding migration energy. (e) Diagram showing the Li^+ diffusion path at the Si/ZnO interface and (f) the corresponding migration energy. (g) Diagram showing another Li^+ diffusion path at the Si/ZnO interface and the (h) corresponding migration energy.

firmed by their low interface energy of −0.43 eV $Å^{-2}$. Some of the Zn–O bonds broke at the interface, with oxygen atoms moving towards the silicon surface to form Si–O bonds. Significant electron depletion around O atoms and charge accumulation around Si atoms were observed at the interface from the charge density difference analysis (Fig. 5b). This clearly indicates the formation of strong Si–O bonds. Interestingly, due to the broken Zn–O bonds, a large channel formed at the interface, serving as a possible path for the rapid transport of lithium ions, which will be discussed in the following part.

To understand the Li^+ transport mechanism at the atomic level, different diffusion paths have been simulated using the NEB method. For the Si(111) surface, the diffusion barriers of various pathways were relatively close, approximately 1 eV. Fig. 5c and d present only one example; other pathways and their corresponding diffusion barriers can be found in Fig. S16. For the Si/ZnO interface, the diffusion paths across and along (Fig. 5g) the channel mentioned above have been calculated (Fig. 5e). Obviously, the diffusion barrier along the channel (about 0.5 eV) was significantly lower than that across channels (about 1.1 eV) or on the Si(111) surface (Fig. 5f and h). As predicted, the channel at the ZnO/Si interface serves as the primary mechanism for the rapid transport of lithium ions, which results from the structural reconstruction at the interface.

To demonstrate the feasibility of Si–ZnO_4 as high-energy and high-power electrode for emerging ASSLBs, a prototype full cell was assembled using coupled Si–ZnO_4 as the negative electrode and commercial NCM811 as the positive electrode, with N/P ratio of 1.1. The electrochemical performance of this full cell was tested at room temperature. Fig. 6a shows the galvanostatic charge and discharge profiles of the full cell at the first two cycles at a rate of 0.1C, with a cut-off voltage range of 2.5 to 4.3 V. The full cell yielded a high reversible discharge specific capacity of 185 mAh g^{-1} with an initial coulombic efficiency of 77%. Fig. 6b shows the rate performance of the full cell at various charge/discharge rates. The full cell yielded discharge capacities of 169 mAh g^{-1}, 150 mAh g^{-1}, 126 mAh g^{-1} and 108 mAh g^{-1} at 0.2C, 0.5C, 1C and 1.5C, respectively. By amplifying the rate 20 times (2C), this full cell still delivered a specific capacity of 92 mAh g^{-1} with a high capacity retention of 49.7%, demonstrating excellent rate capacity. In contrast, full cell based on the pure Si anode delivered a specific capacity of only 42 mAh g^{-1} at 2C with a low capacity retention of 22.9%, which demonstrates that the introduction of ZnO into the Si anode significantly enhanced the rate performance of the full cell. This confirms that the DFT theoretical calculations demonstrate that the rapid Li^+ transport rate ensures its excellent kinetic performance. Furthermore, the full cell based on the Si–ZnO_4 anode can stably operate over 200 cycles at 0.5C with a capacity retention of 71% (Fig. 6c), which is apparently better than full cell based on pure Si anode. Notably, the galvanostatic charge and discharge curves

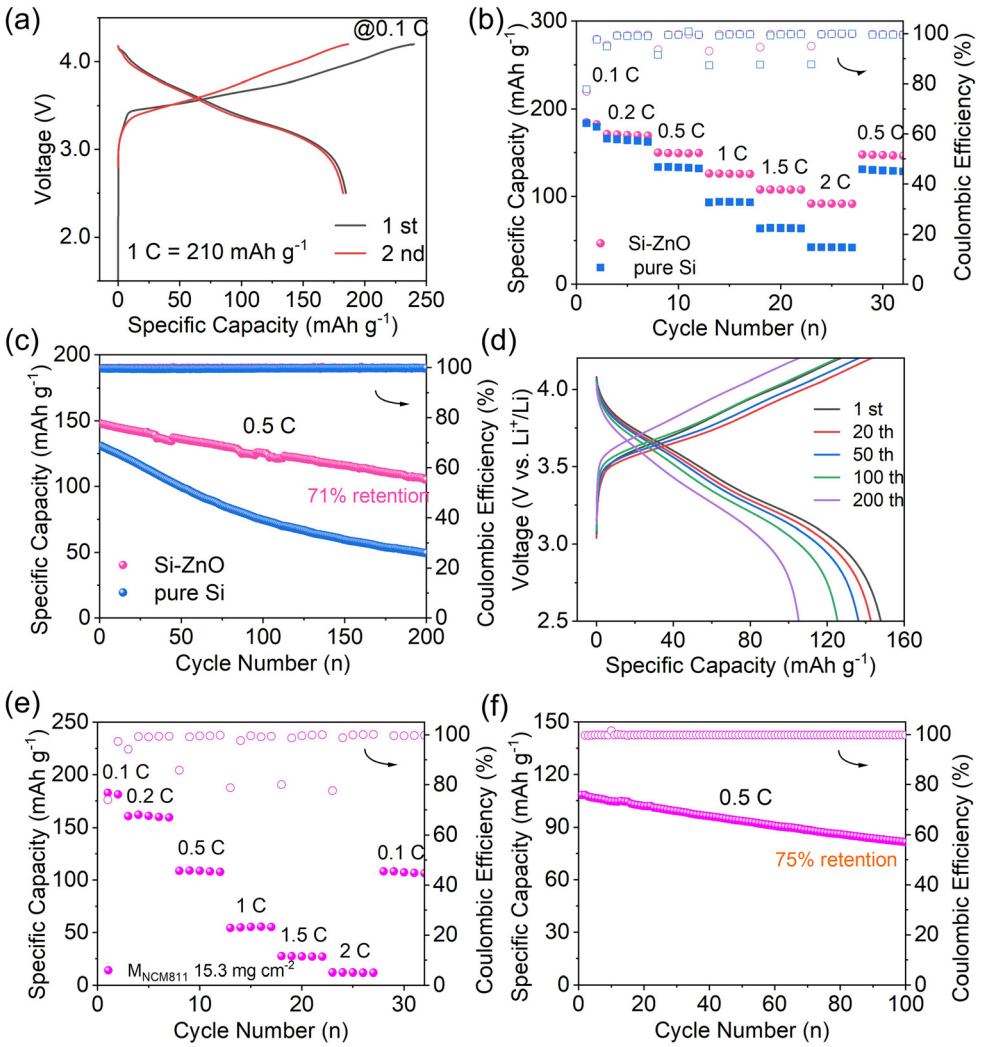

Fig. 6 Electrochemical performance of the Si–ZnO_4/$Li_{5.5}PS_{4.5}Cl_{1.5}$/NCM811 full cell at room temperature. (a) Galvanostatic charge and discharge profiles for the first two cycles. (b) Rate performance. (c) Cycling performance. (d) Galvanostatic charge and discharge profiles during cycling at 0.5C. (e) Rate performance with high mass loading and the (f) corresponding cycling performance at 0.5C.

(Fig. 6d) still preserved the shape of typical NCM cathode during cycling without the phenomena such as soft short circuit. In addition, during the whole cycling test, the Coulomb efficiency of the full cell was close to 100%. To further demonstrate the advantage of the Si–ZnO anode in fabricating ASSLBs, ASSLBs with a high NCM811 loading of 15 mg cm^{-2} were fabricated. This full cell (Fig. 6e) exhibited a reversible discharge capacity of 183 mAh g^{-1}, 159 mAh g^{-1}, 108 mAh g^{-1}, and 55 mAh g^{-1} at 0.1C, 0.2C, 0.5C, and 1C, respectively. Meanwhile, the full cell operated stably over 100 cycles at 0.5C, with a capacity retention of 75% (Fig. 6f).

Conclusions

In summary, we demonstrated a facile and cheap strategy to improve the rate capability and cycling performance of Si anode by adding ZnO nanoparticles into Si microsheets. Various analytical methods, including *ex situ* XRD, TEM, and SEM and *in situ* GEIS tests, revealed that introducing ZnO enables uniform lithium-ion flux distributions at interfaces due to the *in situ* formation of a mixed ion- and electron-conducting Zn/LiZn and Li_2O. Benefiting from improved Li diffusion kinetics in the Si–ZnO composite, the Si–ZnO_4 anode exhibited a reversible discharge capacity of 1125 mAh g^{-1} at a high current density of 5 A g^{-1} in a half cell, suggesting a favorable rate capability. Furthermore, the Si–ZnO_4 anode could be cycled stably over 200 cycles at 0.8 A g^{-1}, with a capacity retention of 76%, demonstrating an excellent long-term cycle life. In addition to the half-cell test, the full-cell test exhibited a specific capacity of 185 mAh g^{-1} at 0.1C and a high-rate capability over 2C as well as over 200 cycles at 0.2C, with a capacity retention rate of 71%. In view of the cost-effective and simple synthesis route and excellent electrochemical performance

achieved by the Si–ZnO anode, it is expected to open up new avenues for the design and development of Si anodes in ASSLBs with high energy density and robust cycling stability in the future.

Experimental section

All chemicals were of analytical grade and used directly without any purification. Zinc acetate ($C_4H_6O_4Zn{\cdot}2H_2O$), *N*,*N*-dimethylformamide (DMF), and Si powder (1 μm) were purchased from Aladdin Scientific Corp. Metal Li was purchased from Guangdong Canrd New Energy Technology Co., Ltd. NCM811 was purchased from Ningbo Ronbay New Energy Technology Co., Ltd.

Preparation of Si–ZnO composite sample

Typically, 0.125 g of zinc acetate was firstly dissolved in a beaker containing 75 mL of *N*,*N*-dimethylformamide (DMF) under vigorous stirring. Then, 0.5 g of commercial Si powder (μ-Si, 1–3 μm) was dispersed into the above DMF solution under vigorous stirring for more than 30 min. Subsequently, the above beaker was sealed with a plastic wrap and then heated at 90 °C for 1 h. After that, the plastic wrap was taken off, and the mixture was heated until the DMF evaporated. The mixed powder was transferred into an oven and heated at 260 °C for 2 h under an air atmosphere. Subsequently, the mixed powder was further pyrolyzed at 700 °C for 1 h at a heating rate of 5 °C min^{-1} under an argon atmosphere. Finally, the product was ground into the final Si–ZnO power. For comparison, composites with different ZnO contents were prepared using the same procedure by adding different concentrations of zinc acetate. For example, the mass ratios of zinc acetate/Si precursor were set to 1 : 2 and 1 : 8, which were denoted as Si–ZnO_x powder (where x represents the mass ratio of zinc acetate/Si). The $Li_{5.5}PS_{4.5}Cl_{1.5}$ electrolyte (LPSCl) was prepared using a sintering method according to our previous study.[6]

Material characterization

X-ray diffraction (XRD) patterns were obtained from a SmartLab 9-KW diffractometer with Cu K_α radiation (Japan) and a scanning range between 10° and 80°. Raman spectral analysis was performed using a JY-HR800 micro-Raman spectrometer (France) with an excitation wavelength of 532 nm. The morphology and structure of Si–ZnO powder were characterized *via* scanning electron microscopy (SEM, JSM-7800F, Hitachi, Japan) and transmission electron microscopy (TEM, JEM-F200, JEOL, Japan). The cross-section SEM images of Si–ZnO electrode in Fig. 4a-c were obtained by frozen in liquid nitrogen and then cut using a scalpel. X-ray photoelectron spectroscopy (XPS, PerkinElmer PHI-5702 Spectrometer, USA) with Al K_α radiation was used to explore chemical composition of Si–ZnO powder. Inductively coupled plasma (ICP) atomic emission spectroscopy measurements were confirmed on an Optima 7300 DV.

Electrode preparation

Si–ZnO_x (98 wt%) and polyvinylidene fluoride (PVDF; 2 wt%) dissolved in methyl-2-pyrrolidone (NMP) were mixed in a mortar. The slurry was then homogeneously painted on the current collector (Cu foil) using a blade and dried at 80 °C under vacuum for 6 h. The foil was punched into round electrodes with a diameter of 8 mm. The active mass loading of Si–ZnO on Cu foil was 0.6–1.3 mg. The electrode thickness was 22 μm.

Cell assembly

For half-cells, the LPSCl (100 mg, 800 μm) electrolyte was pressed at 310 MPa for 3 minutes in a hollow cylinder mold with a diameter of 10 mm. Then, the Li–In metal foil with a diameter of 10 mm was placed on an electrolyte pellet. Li–In metal foil was prepared by sticking an Li metal foil (5 mg) on a metal In foil (120 mg). Then, the Si–ZnO electrode coated on the Cu foil was placed on the other side of the electrolyte pellet. The current for a half-cell should be set to 0.8 times the mass of the Si–ZnO composite material, which is the mass of silicon in it. For Si||NCM811 full cells, the composite cathode was mixed with NCM811, LPSCl and VGCF (vapor growth carbon fiber) with a mass ratio of 65 : 30 : 5 for 30 min in an agate mortar by hand. Then, 100 mg of LPSCl electrolyte was pressed onto a sheet under a pressure of 1 ton for 1 minute. Next, the composite cathode powder was uniformly spread on one side of the electrolyte layer and pressed at 310 MPa for 3 minutes. The thickness of the positive NCM electrode was 100 μm. Finally, the Si–ZnO electrode was placed on the other side of the electrolyte layer, and the three-layer cell was sandwiched between two stainless-steel rods. The N/P ratio was ~1.1. All cells were heated at 60 °C overnight before tests. The cells were tested under a pressure of 300 MPa. All assembling processes were carried out in an argon-filled glovebox.

Electrochemical performance tests

Cyclic voltammetry (CV) tests, galvanostatic charge/discharge (GCD) measurements, and electrical impedance spectroscopy (EIS) tests were recorded using CHI760E (Shanghai, China) and/or a Land CT2001A battery test system (Wuhan Land Electronics, Ltd, China).

Theoretical method

All first-principles simulations in this study were performed using the Vienna Ab Initio Simulation Package (VASP) for periodic density functional theory (DFT) calculations,[39,40] employing the generalized gradient approximation (GGA) to describe the exchange–correlation effects, alongside the Perdew, Burke and Ernzerhof (PBE) exchange–correlation functional.[41] The ion cores were represented by the projector augmented wave (PAW) potential constructed by Kresse and Joubert.[42,43] Energy calculations were performed in the first Brillouin zone using 9 × 9 × 1 *k*-points in the Monkhorst–Pack scheme. The energy cutoff value was set to 520 eV. All atomic forces were set to 0.01 eV $Å^{-1}$, and the energy convergence accuracy was set to less

than 1.0×10^{-5} eV per atom. The convergence of the results with respect to these parameters has been carefully checked.

For the calculation of each crystal plane,[44] the slab model was used to simulate the surface with a 20 Å vacuum. The interface energy was calculated as follows:

$$E_{\text{interface}} = E_{\text{tot}} - E_{\text{slab A}} - E_{\text{slab B}}$$

where E_{tot} and E_{slab} were the total energy of the interface system and established slab models, respectively.

To further investigate the diffusion paths, the nudged elastic band method (NEB) was employed,[45] which is an automatic search routine for finding the energy minimum path between specified initial and final states.

Conflicts of interest

The authors declare no conflict of interest.

Data availability

The data supporting this article have been included as part of the supplementary information (SI). Supplementary information is available. See DOI: https://doi.org/10.1039/d5eb00238a.

Acknowledgements

This work was supported by the National Key R&D Program of China (2024YFA1211104), the National Natural Science Foundation of China (52272224 and 52572241) and the Science Fund of Shandong Laboratory of Advanced Materials and Green Manufacturing at Yantai (AMGM2024F26).

References

1 A. Manthiram, X. Yu and S. Wang, *Nat. Rev. Mater.*, 2017, **2**, 16103.
2 C. Wang, J. Liang, J. T. Kim and X. Sun, *Sci. Adv.*, 2022, **8**, eadc9516.
3 W. Yu, N. Deng, Y. Feng, X. Feng, H. Xiang, L. Gao, B. Cheng, W. Kang and K. Zhang, *eScience*, 2024, **5**, 100278.
4 Z.-Y. Wang, C.-Z. Zhao, S. Sun, Y.-K. Liu, Z.-X. Wang, S. Li, R. Zhang, H. Yuan and J.-Q. Huang, *Matter*, 2023, **6**, 1096.
5 F. Ren, Z. Liang, W. Zhao, W. Zuo, M. Lin, Y. Wu, X. Yang, Z. Gong and Y. Yang, *Energy Environ. Sci.*, 2023, **16**, 2579.
6 S. Zhang, J. Chen, C. Zhu, Q. Liu, Q. Li, R. Liu, X. Jiang, Y. Yan, S. Sun, L. Yin and R. Wang, *ACS Nano*, 2023, **17**, 24290.
7 S. Kalnaus, N. J. Dudney, A. S. Westover, E. Herbert and S. Hackney, *Science*, 2023, **381**, 6664.
8 J. A. Lewis, K. A. Cavallaro, Y. Liu and M. T. McDowell, *Joule*, 2022, **6**, 1418.
9 M. Zhao, J. Zhang, C. M. Costa, S. Lanceros-Méndez, Q. Zhang and W. Wang, *Adv. Mater.*, 2023, **36**, e2308590.
10 H. Huo and J. Janek, *ACS Energy Lett.*, 2022, **7**, 4005.
11 H. Huo, M. Jiang, Y. Bai, S. Ahmed, K. Volz, H. Hartmann, A. Henss, C. V. Singh, D. Raabe and J. Janek, *Nat. Mater.*, 2024, **23**, 543.
12 D. H. S. Tan, Y.-T. Chen, H. Yang, W. Bao, B. Sreenarayanan, J.-M. Doux, W. Li, B. Lu, S.-Y. Ham, B. Sayahpour, J. Scharf, E. A. Wu, G. Deysher, H. E. Han, H. J. Hah, H. Jeong, J. B. Lee, Z. Chen and Y. S. Meng, *Science*, 2021, **373**, 1494.
13 H. Zhao, F. Yang, C. Li, T. Li, S. Zhang, C. Wang, Z. Zhang and R. Wang, *ChemPhysMater*, 2023, **2**, 1.
14 Y. Li, Q. Li, J. Chai, Y. Wang, J. Du, Z. Chen, Y. Rui, L. Jiang and B. Tang, *ACS Mater. Lett.*, 2023, **5**, 2948.
15 D. Cao, T. Ji, A. Singh, S. Bak, Y. Du, X. Xiao, H. Xu, J. Zhu and H. Zhu, *Adv. Energy Mater.*, 2023, **13**, 2203969.
16 L. Ye, Y. Lu, Y. Wang, J. Li and X. Li, *Nat. Mater.*, 2024, **23**, 244.
17 W. Yan, Z. Mu, Z. Wang, Y. Huang, D. Wu, P. Lu, J. Lu, J. Xu, Y. Wu, T. Ma, M. Yang, X. Zhu, Y. Xia, S. Shi, L. Chen, H. Li and F. Wu, *Nat. Energy*, 2023, **8**, 800.
18 X. Han, M. Xu, L.-H. Gu, C.-F. Lan, M.-F. Chen, J.-J. Lu, B.-F. Sheng, P. Wang, S.-Y. Chen and J.-Z. Chen, *Rare Met.*, 2023, **43**, 1017.
19 T. K. Schwietert, V. A. Arszelewska, C. Wang, C. Yu, A. Vasileiadis, N. J. J. de Klerk, J. Hageman, T. Hupfer, I. Kerkamm, Y. Xu, E. van der Maas, E. M. Kelder, S. Ganapathy and M. Wagemaker, *Nat. Mater.*, 2020, **19**, 428.
20 D. H. S. Tan, E. A. Wu, H. Nguyen, Z. Chen, M. A. T. Marple, J.-M. Doux, X. Wang, H. Yang, A. Banerjee and Y. S. Meng, *ACS Energy Lett.*, 2019, **4**, 2418.
21 Z. Wang, X. Shen, S. Chen, R. Qiao, B. Sun, J. Deng and J. Song, *Adv. Mater.*, 2024, **36**, 2405025.
22 S. Behera, S. Ippili, V. Jella, N. Y. Kim, S. C. Jang, J. W. Jung, S. G. Yoon and H. S. Kim, *Energy Environ. Mater.*, 2024, **7**, e12734.
23 X. H. Huang, R. Q. Guo, J. B. Wu and P. Zhang, *Mater. Lett.*, 2014, **122**, 82.
24 J. E. Cloud, Y. Wang, X. Li, T. S. Yoder, Y. Yang and Y. Yang, *Inorg. Chem.*, 2014, **53**, 11289.
25 T. Schott, R. Robert, S. P. Benito, P. A. Ulmann, P. Lanz, S. Zürcher, M. E. Spahr, P. Novák and S. Trabesinger, *J. Phys. Chem. C*, 2017, **121**, 25718.
26 T. Gruber, D. Thomas, C. Röder, F. Mertens and J. Kortus, *J. Raman Spectrosc.*, 2013, **44**, 934.
27 E. Park, H. Yoo, J. Lee, M.-S. Park, Y.-J. Kim and H. Kim, *ACS Nano*, 2015, **9**, 7690.
28 C. Shen, X. Fang, M. Ge, A. Zhang, Y. Liu, Y. Ma, M. Mecklenburg, X. Nie and C. Zhou, *ACS Nano*, 2018, **12**, 6280.
29 Y. He, L. Jiang, T. Chen, Y. Xu, H. Jia, R. Yi, D. Xue, M. Song, A. Genc, C. Marquis, L. Pullan, T. Tessner, J. Yoo, X. Li, J. Zhang, S. Zhang and C. Wang, *Nat. Nanotechnol.*, 2021, **16**, 1113.

30 Y. Sohn, J. Oh, J. Lee, H. Kim, I. Hwang, G. Noh, T. Lee, J. Y. Kim, K. Y. Bae, T. Lee, N. Lee, W. J. Chung and J. W. Choi, *Adv. Mater.*, 2024, **36**, 2407443.
31 J. Yu, Q. Liu, X. Hu, S. Wang, J. Wu, B. Liang, C. Han, F. Kang and B. Li, *Energy Storage Mater.*, 2022, **46**, 68.
32 L. Zhang, Q. Meng, Y. Dai, X. Feng, M. Shen, Q. Zhuang, Z. Ju, R. Zheng, Z. Wang, Y. Cui, H. Sun and Y. Liu, *Nano Energy*, 2023, **113**, 108573.
33 K. Yan, Z. Lu, H.-W. Lee, F. Xiong, P.-C. Hsu, Y. Li, J. Zhao, S. Chu and Y. Cui, *Nat. Energy*, 2016, **1**, 16010.
34 L. Zhao, T. Wang, F. Zuo, Z. Ju, Y. Li, Q. Li, Y. Zhu, H. Li and G. Yu, *Nat. Commun.*, 2024, **15**, 3778.
35 G. M. Hobold, C. Wang, K. Steinberg, Y. Li and B. M. Gallant, *Nat. Energy*, 2024, **9**, 580.
36 R. Guo and B. M. Gallant, *Chem. Mater.*, 2020, **32**, 5525.
37 Y. Lu, C.-Z. Zhao, J.-Q. Huang and Q. Zhang, *Joule*, 2022, **6**, 1172.
38 K. Takayanagi, Y. Tanishiro, M. Takahashi and S. Takahashi, *Surf. Sci.*, 1985, **164**, 367.
39 G. Kresse and J. Furthmuller, *Phys. Rev. B: Condens. Matter Mater. Phys.*, 1996, **54**, 11169.
40 G. Kresse and J. Furthmuller, *Comp. Mater. Sci.*, 1996, **6**, 15.
41 J. P. Perdew, K. Burke and M. Ernzerhof, *Phys. Rev. Lett.*, 1996, **77**, 3865.
42 P. Blochl, *Phys. Rev. B: Condens. Matter Mater. Phys.*, 1994, **50**, 17953.
43 G. Kresse and D. Joubert, *Phys. Rev. B: Condens. Matter Mater. Phys.*, 1999, **59**, 1758.
44 K. Mathew, R. Sundararaman, K. Letchworth-Weaver, T. A. Arias and R. G. Hennig, *J. Chem. Phys.*, 2014, **140**, 084106.
45 G. Henkelman and H. Jonsson, *J. Chem. Phys.*, 2000, **113**, 9978.
46 S. Wen, Z. Sun, X. Wu, S. Zhou, Q. Yin, H. Chen, J. Pan, Z. Zhang, Z. Zhuang, J. Wan, W. Zhou, D. Peng and Q. Zhang, *Adv. Funct. Mater.*, 2025, **35**, 2422147.
47 Z. Sun, Q. Yin, S. Zhou, H. Chen, S. Wen, H. Yang, X. Wu, J. Pan, J. Han, H. Yang, Z. Zhuang, S. Feng, L. Zhang, D. Peng and Q. Zhang, *Adv. Energy Mater.*, 2025, **15**, 2500189.
48 Z. Sun, Z. Zhang, S. Zhou, W. Liu, J. Liu, Q. Yin, J. Pan, X. Wu, Z. Zhuang, D. Peng and Q. Zhang, *J. Materiomics*, 2025, **11**, 101053.
49 Z. Sun, Q. Yin, H. Chen, M. Li, S. Zhou, S. Wen, J. Pan, Q. Zheng, B. Jiang, H. Liu, K. Kim, J. Li, X. Han, Y. He, L. Zhang, M. Li and Q. Zhang, *Interdiscip. Mater.*, 2023, **2**, 635–663.